Parallel algorithm for multiscale atomistic/continuum simulations using LAMMPS

2015 Modelling Simul. Mater. Sci. Eng. 23 055002

(http://iopscience.iop.org/0965-0393/23/5/055002)

IOP Publishing Modelling and Simulation in Materials Science and Engineering

Modelling Simul. Mater. Sci. Eng. **23** (2015) 055002 (23pp) doi:10.1088/0965-0393/23/5/055002

Parallel algorithm for multiscale atomistic/continuum simulations using LAMMPS

F Pavia and W A Curtin

Institute of Mechanical Engineering, EPFL, 1015 Lausanne, Switzerland

E-mail: fabio.pavia@epfl.ch

Received 2 December 2014, revised 27 March 2015
Accepted for publication 6 April 2015
Published 15 May 2015

Abstract

Deformation and fracture processes in engineering materials often require simultaneous descriptions over a range of length and time scales, with each scale using a different computational technique. Here we present a high-performance parallel 3D computing framework for executing large multiscale studies that couple an atomic domain, modeled using molecular dynamics and a continuum domain, modeled using explicit finite elements. We use the robust Coupled Atomistic/Discrete-Dislocation (CADD) displacement-coupling method, but without the transfer of dislocations between atoms and continuum. The main purpose of the work is to provide a multiscale implementation within an existing large-scale parallel molecular dynamics code (LAMMPS) that enables use of all the tools associated with this popular open-source code, while extending CADD-type coupling to 3D. Validation of the implementation includes the demonstration of (i) stability in finite-temperature dynamics using Langevin dynamics, (ii) elimination of wave reflections due to large dynamic events occurring in the MD region and (iii) the absence of spurious forces acting on dislocations due to the MD/FE coupling, for dislocations further than 10 Å from the coupling boundary. A first non-trivial example application of dislocation glide and bowing around obstacles is shown, for dislocation lengths of ∼50 nm using fewer than 1 000 000 atoms but reproducing results of extremely large atomistic simulations at much lower computational cost.

Keywords: multiscale, atomistic, dislocations, LAMMPS, finite elements

(Some figures may appear in colour only in the online journal)

1. Introduction

Deformation and fracture processes in engineering materials combine complex phenomena such as dislocation motion and interaction with crack tips and other material defects and

involve a wide range of length and time scales. In some problems, a separation of scales is possible so that small-scale studies can provide input parameters to larger-scale models. In other cases, a separation of scales is not feasible due to strong coupling across scales, such as in fracture in metals where material separation is an atomic scale event but with the crack tip conditions controlled by plastic flow via dislocations over much larger scales. The use of concurrent multiscale methodologies is essential to capture the interactions among the different scales in such cases. Concurrent methods also eliminate boundary condition effects (image forces) that exist in finite-size atomistic simulations. Concurrent methods link entirely different material descriptions, i.e. quantum mechanical, atomistic, discrete dislocations and/or continuum plasticity, yet must be free of spurious forces. Over the last 15 years a number of multiscale methods have been developed to obtain quantum or atomic accuracy at a tiny fraction of the computational cost of a comparable-size single-scale simulation. The coupling of atomistic models to continuum elasticity has received the most attention and many existing methods have been benchmarked by Miller and Tadmor [1, 2]. Recent work has improved the accuracy of some methods [4, 5]. Most existing methods are limited to 2D or small 3D cases running in serial computations and remain within the domain of research codes that are difficult to export to the broader community. When considering 3D dislocation problems (i.e. problems with long-range elastic fields), the number of mesh elements and nodes required to reproduce the accurate deformation at the continuum/atomistic interface is several orders of magnitude larger than that needed for simple 2D models. Such 3D sizes prevent the use of standard matrix factorization and inversion techniques in the continuum region. A high-performance parallel 3D computing framework for large multiscale studies thus requires explicit dynamics methods. As done in 2D by Shiari *et al* [6], here we develop an explicit Velocity-Verlet finite-element scheme with a lumped-mass approach to model a large 3D continuum region; this requires only matrix-vector and vector–vector operations and is easily parallelizable across several CPUs. We demonstrate a method that uses one of the most accurate coupling methods, CADD [1, 2], extended to 3D and operating within the framework of the large-scale parallel molecular dynamics code LAMMPS [3]. While different particle-continuum hybrid methods exist in the literature, those are not easily accessible in general for further developments to a wide array of researchers. In this paper, our main goal is to describe in detail the implementation of the CADD displacement-coupling multiscale scheme using LAMMPS as the atomistic driver with an associated FEM add-on, which will provide an accurate, high-performance multiscale method to the wide community of researchers in materials modeling.

The remainder of this paper is organized as follows. In section 2, we review for completeness the CADD coupling method, the resulting energy functionals and forces on degrees of freedom and the formal integration scheme for the dynamics of each degree of freedom. In section 3, we describe how the coupled method is integrated within LAMMPS, including parallelization of the FEM and provide an overall description of the algorithms. In section 4, we present the details of the mesh generation method used to build the FEM mesh starting from the atomistic crystal structure and with periodic boundary conditions. Section 5 provides validation and verification of the method and application to the planar bow-out of a pinned dislocation in a full 3D atomistic domain.

2. Review of CADD atom/continuum coupling method

As shown in the schematic of figure 1(a), the CADD coupling method [7–9] divides the entire body of interest into two regions: a fully atomistic domain Ω^A and a continuum domain Ω^C. A transition pad Ω^P, included within the continuum domain Ω^C, assists in providing error-free

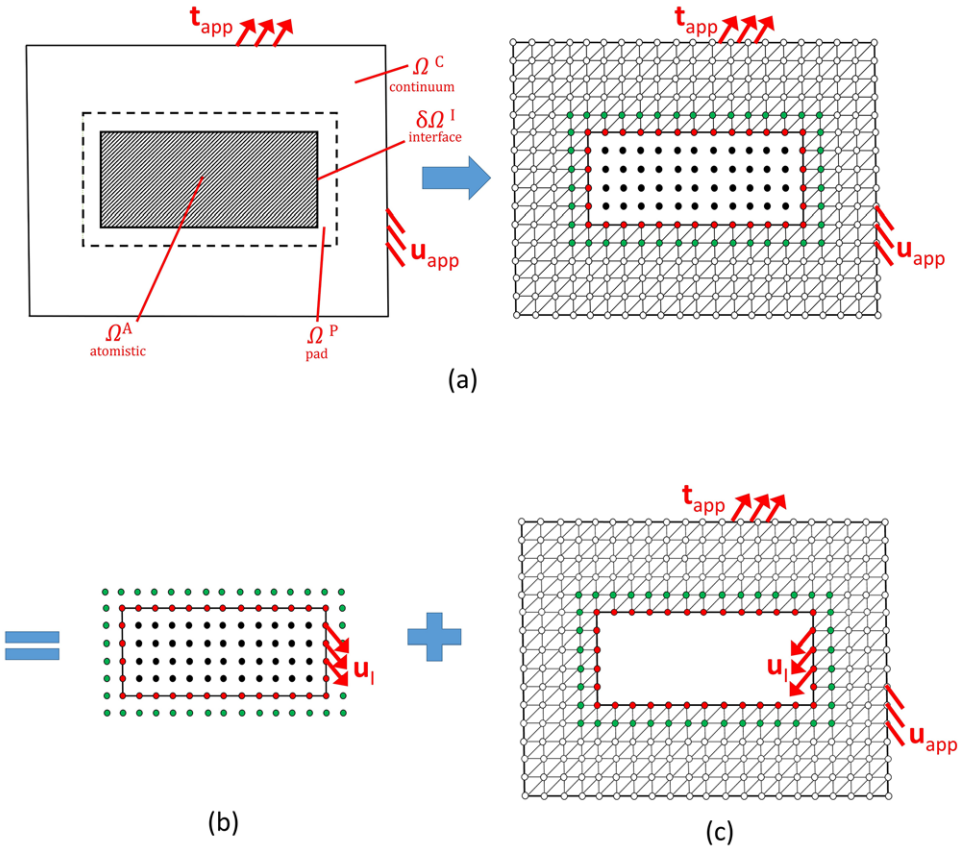

Figure 1. (a) Division of the body of interest into two regions studied with different modeling techniques: fully atomistic Ω^A and continuum finite element region Ω^C. A transition pad Ω^P, included within Ω^C, is at the interface with both atomistic and continuum descriptions. Displacements $\mathbf{u}_{\text{app}}$ and tractions $\mathbf{t}_{\text{app}}$ are applied on the outer boundary of the body. The atomistic (b) and continuum (c) domains are coupled through the displacements $\mathbf{u}_I$ of the interface nodes/atoms along $\delta\,\Omega^I$ (in red) between Ω^A and Ω^P. The pad nodes/atoms (in green) interact with the atoms of the fully atomistic region Ω^A to give a full complement of neighbors but move according to displacements computed by the continuum FE method.

coupling as described below. We denote the atom/continuum interface as a domain $\delta\,\Omega^I$ that is shared by both Ω^A and Ω^P. Displacement continuity is enforced by having nodes and atoms coincident along $\delta\,\Omega^I$. The pad nodal positions are treated entirely within the continuum FE approximation but are also used as atomic positions in the atomistic analysis to transmit forces from the continuum to the atomistic domain. Thus, two independent potential energy functionals, W^C and W^{A+P}, are used to model the deformations in the overlapping domains Ω^C and Ω^{A+P}.

The energy functional for atoms in the fully atomistic and for atoms in the pad is written as

$$W^{A+P} = \sum_{i \in \Omega^A, \Omega^P} E^i, \tag{1}$$

where E^i is the potential energy of atom i as computed using the semi-empirical interatomic potential chosen to describe the atomic system. This energy functional is usually non-local

since the atomic interactions are often many-body and extending beyond near neighbors. Interaction forces on atom i in Ω^A are computed from W^{A+P} as the derivative with respect to the atom position $\mathbf{r_i}$ of the energy functional, as in

$$\mathbf{F}^i = -\frac{\partial}{\partial \mathbf{r}^i}(W^{A+P}). \qquad i \in \Omega^A \text{ only} \tag{2}$$

External forces $\mathbf{F}^i_{\text{ext}}$ may also be applied to the atoms. Note that interface atoms in $\delta\,\Omega^I$ are contained within Ω^A and so have fully atomistically-derived forces even though many atomic neighbors are in the pad region. Atomistic forces are *not* computed on the pad atoms in Ω^P.

For the domain Ω^C, a continuum strain energy density function $W[\mathbb{F}(\mathbf{r})]$ is defined as a function of the spatially-varying deformation gradient $\mathbb{F}(\mathbf{r})$. The energy for the continuum domain Ω^C is obtained by integrating $W[\mathbb{F}(\mathbf{r})]$ over the volume

$$W^C = \int_{\Omega^C} W[\mathbb{F}(\mathbf{r})]\mathrm{d}\Omega. \tag{3}$$

Linear elasticity is used to describe this region, so that the strain energy density at position $\mathbf{r}$ can be written in index notation as

$$W(\mathbf{r}) = \frac{1}{2}\epsilon_{ij}(\mathbf{r})\epsilon_{kl}(\mathbf{r})C_{ijkl}, \tag{4}$$

with C_{ijkl} the elastic modulus tensor corresponding to the atomistic material, $\epsilon_{ij}(\mathbf{r}) = \frac{1}{2}[\nabla\mathbf{u} + (\nabla\mathbf{u})^T]$ the strain tensor and $\mathbf{u}$ the displacement field at position $\mathbf{r}$. The continuum region is then discretized into a mesh of n_{elem} finite elements and n_{node} nodes. Equation (3) can then be written as

$$W^C = \frac{1}{2}\sum_{e=1}^{n_{\text{elem}}}\int_{V_e}\mathbf{U}_e^T\mathbb{B}^T\mathbb{D}\mathbb{B}\mathbf{U}_e\mathrm{d}V, \tag{5}$$

where V_e is the volume of element e, $\mathbb{B}$ and $\mathbb{D}$ are the element deformation matrix and the constitutive relation matrix as defined in [10] and $\mathbf{U}_e$ is the nodal displacement vector of each element calculated from an undeformed reference configuration. The force $\mathbf{F}^i$ on the ith node at position $\mathbf{r}^i$ is then computed from the derivative of the energy with respect to nodal position as

$$\mathbf{F}^i = -\frac{\partial}{\partial \mathbf{r}^i}(W^C), \qquad i \in \Omega^C \tag{6}$$

Nodal forces on all the continuum degrees of freedom can be combined into a single vector for the entire mesh, $\mathbf{F} = [\mathbf{F}^1; ...; \mathbf{F}^{n_{\text{node}}}]$, determined as in [10] from the nodal displacements $\mathbf{U}_e$ deforming each element e

$$\mathbf{F} = \sum_{e=1}^{n_{\text{elem}}}\int_{V_e}\mathbb{B}^T\mathbb{D}\mathbb{B}\mathbf{U}_e\mathrm{d}V. \tag{7}$$

External forces $\mathbf{F}^e_{\text{ext}}$ are also added on the nodes of each element e with faces Γ^e on the outer boundaries $\partial\Omega^C$ of the continuum region corresponding to imposed applied tractions $\mathbf{t}_{\text{app}}$ as

$$\mathbf{F}^e_{\text{ext}} = \int_{\Gamma^e}\mathbb{N}^T\mathbf{t}_{\text{app}}\mathrm{d}\Gamma, \tag{8}$$

with $\mathbb{N}$ the matrix of shape functions mapping the element e to a local reference [10].

With the above physical forces, Langevin dynamics is used to impose a desired temperature in the atomistic domain and to facilitate explicit dynamics in the continuum domain.

The total force acting on each degree of freedom (atom or node) in the system is thus computed as

$$\mathbf{F}^i_{\text{tot}} = \mathbf{F}^i + \mathbf{f}^i - \gamma(\mathbf{r}^i) m_i \dot{\mathbf{r}}^i + \mathbf{F}^i_{\text{ext}}. \tag{9}$$

Here, $\gamma(\mathbf{r}^i)$ is a (possibly spatial-varying) damping parameter that determines a frictional (viscous) drag force proportional to the velocity $\dot{\mathbf{r}}^i$ (the dot indicates time derivative $\partial/\partial t$), m_i is the mass and $\mathbf{f}^i = \sqrt{2 m_i \gamma(\mathbf{r}^i) K_{\text{B}} T}\, \eta(t)$ is a random force proportional to the square root of the desired finite temperature T of the system (with k_{B} the Boltzman constant and $\eta(t)$ a delta-correlated stationary Gaussian process with zero-mean satisfying $\langle \eta(t)\, \eta(t') \rangle = \delta(t - t')$). We use the atomic mass for the atoms in the atomistic domain and a nodal lumped-mass, obtained by equally distributing the total mass of each element to its nodes [10], for the continuum nodes. Forces of equation (9) are set to zero for the nodes with applied displacement $\mathbf{u}_{\text{app}}$ on the outer boundary of Ω_C and for the interface nodes on $\delta\, \Omega_I$ to implement the displacement boundary condition $\mathbf{u}_I$ when using an explicit method in the continuum. The nodes at the interface are tied to the interface atoms, which move according to the atomic forces of equations (2) and (9). The periodic faces of the model have the same mesh pattern, so that couples of corresponding nodes with the same in-plane positions can be found. Periodicity can be enforced by transferring the total forces and masses of each node on a periodic face (arbitrarily defined as the 'slave' node) to the corresponding node on the other periodic face (thus defined as the 'master' node). At each time-step the position of the 'slave' node is then imposed as a displacement boundary conditions using the value of displacement of the 'master' node obtained from equation (10).

An explicit scheme is then used to compute the time-evolution of the continuum and atomistic degrees of freedom (nodes and atoms). With $\mathbf{r}^i_{(n)}$, $\dot{\mathbf{r}}^i_{(n)}$ and $\ddot{\mathbf{r}}^i_{(n)}$ indicating the position, velocity and acceleration of the ith node or atom at time step (n), the positions and velocities at the next time step $(n + 1)$ are computed from

$$\mathbf{r}^i_{(n+1)} = \mathbf{r}^i_{(n)} + \Delta t \dot{\mathbf{r}}^i_{(n)} + \frac{\Delta t^2}{2} \ddot{\mathbf{r}}^i_{(n)}, \tag{10}$$

$$\dot{\mathbf{r}}^i_{(n+1)} = \dot{\mathbf{r}}^i_{(n)} + (1 - \alpha) \Delta t \ddot{\mathbf{r}}^i_{(n)} + \alpha \Delta t \ddot{\mathbf{r}}^i_{(n+1)}, \tag{11}$$

where Δt is the time increment between integration steps and α is a parameter equal to 0.5 for the Velocity Verlet scheme used in this work. The positions $\mathbf{r}^i_{(n+1)}$ at the next time step can be immediately found through equation (10). The velocities $\dot{\mathbf{r}}^i_{(n+1)}$ depend on the accelerations at the next step, which are obtained using Newton's second law at time step $(n + 1)$,

$$m_i \ddot{\mathbf{r}}^i_{(n+1)} = \mathbf{F}^i_{\text{tot}(n+1)}, \tag{12}$$

with $\mathbf{F}^i_{\text{tot}(n+1)}$ the total force obtained from equation (9). Since velocities $\dot{\mathbf{r}}^i_{(n+1)}$ are not yet computed when evaluating the total force at the next step $(n + 1)$, drag forces are approximated by evaluating velocities at the half time step $\left(n + \frac{1}{2}\right)$,

$$\dot{\mathbf{r}}^i_{\left(n+\frac{1}{2}\right)} = \dot{\mathbf{r}}^i_{(n)} + \frac{1}{2} \Delta t \ddot{\mathbf{r}}^i_{(n)}. \tag{13}$$

The accelerations $\ddot{\mathbf{r}}^i_{(0)}$ at the beginning of the simulation $(n = 0)$ are found directly from equations (9) and (12) for given initial positions and velocities, $\mathbf{r}^i_{(0)}$ and $\dot{\mathbf{r}}^i_{(0)}$.

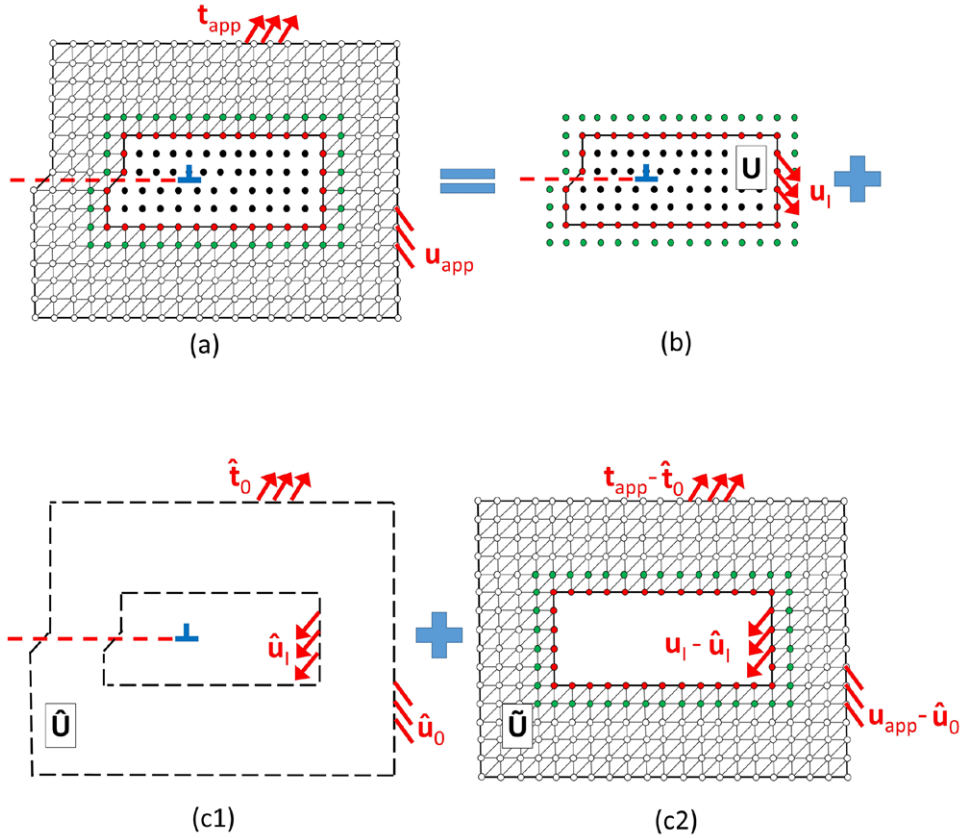

Figure 2. (a) Decomposition of a boundary value problem in which one dislocation (in blue) is present in the atomistic region and displacements $\mathbf{u}_{app}$ and tractions $\mathbf{t}_{app}$ are imposed on the outer boundary of the body. (b) The atomistic region provides a displacement $\mathbf{u}$ field with discontinuities on the dislocation slip plane (red dashed line) at the interface with the continuum region. (c1) Static displacement field $\hat{\mathbf{u}}$ of an individual fixed *ghost* dislocation in an infinite elastic medium imposing tractions and displacements $\hat{\mathbf{t}}_0$, $\hat{\mathbf{u}}_I$ and $\hat{\mathbf{u}}_0$ on the interface and outer boundaries of the body. (c2) Corrective displacement field $\tilde{\mathbf{u}}$ with tractions and displacements of (c1) removed from outer boundaries of the body and at the interface. Superposition of the displacement fields of (c1) and (c2) gives the full solution $\mathbf{u}$ for the continuum region and it is used to update the position of the pad atoms at each simulation step. For atoms and nodes we use the same color scheme of figure 1.

When dislocations are present in the atomistic region, there are discontinuities in the displacement field along the plane of slip in the continuum region, as shown in figure 2(a). Standard linear elastic finite elements can capture only continuous fields and so the displacement discontinuities must be represented analytically, subtracted from the finite element problem and then superimposed with the finite element solution to obtain the full solution. As depicted in the schematic of figure 2, this procedure is identical to that of Van der Giessen and Needleman [11], where two subproblems are superposed to obtain the total displacement $\mathbf{u}$ from the reference undeformed configuration, figures 2(c1) and (c2). The first problem considers the static field of an individual fixed *ghost* dislocation in an infinite elastic medium and has an analytic solution $\hat{\mathbf{u}}$. This field imposes tractions and displacements $\hat{\mathbf{t}}_0$, $\hat{\mathbf{u}}_I$ and $\hat{\mathbf{u}}_0$ on

the interface $\delta\,\Omega_I$ and the outer boundaries of Ω^C. The second problem solves for the continuous displacement field $\tilde{\mathbf{u}}(t)$ given the corrective boundary conditions $\mathbf{u}_I - \hat{\mathbf{u}}_I$, $\mathbf{u}_{\text{app}} - \hat{\mathbf{u}}_0$ and $\mathbf{t}_{\text{app}} - \hat{\mathbf{t}}_0$, where $\mathbf{u}_I$, $\mathbf{u}_{\text{app}}$ and $\mathbf{t}_{\text{app}}$ are respectively the displacement at the interface $\partial\Omega^A$ and the imposed displacements and tractions on $\partial\Omega^C$. Explicit finite elements dynamics is used to obtain this solution. The total displacement field for the continuum region is then $\mathbf{u} = \hat{\mathbf{u}} + \tilde{\mathbf{u}}$. Note that since $\hat{\mathbf{u}}$ is a static displacement field, $\dot{\hat{\mathbf{u}}} = \ddot{\hat{\mathbf{u}}} = 0$. The choice of the analytic field $\hat{\mathbf{u}}$, first removed and then added back to obtain the full solution, is arbitrary aside from containing the correct displacement discontinuity due to the dislocation. So, the analytic field of the ghost dislocation can be described by the isotropic Volterra solution [11–14] or by the fully-anisotropic fields using the classical sextet anisotropic elasticity theory [15].

3. Implementation

We implement the above algorithm within LAMMPS [3] since this open-source code computes interatomic forces according to equation (2) for a wide variety of atomic potentials and can perform efficient and scalable parallel molecular dynamics simulations over large domains with millions of degrees of freedom. The LAMMPS code has a modular structure composed of separate subroutines allowing for easy implementation of new features. New subroutines (defined with the term *fix* inside LAMMPS) are initialized at the beginning of a simulation and, having access to the values of atomic positions, velocities and displacements from a reference configuration, are called iteratively before and after calculation of forces to integrate the equations of motion for all the atoms according to the explicit scheme of equations (10) and (11) or to realize other tasks.

Standard LAMMPS automatically distributes the atoms of the fully atomistic and pad region to the available processors, calculates atomic interactions for each configuration and updates the positions of the full atoms during the simulations. Implementation of the coupling between the atomistic region and the continuum region as in figure 1 requires the development of subroutines realizing the following tasks at each time step: (I) store and update positions, velocities and accelerations of continuum nodal degrees of freedom, (II) compute forces on the FE nodes using equation (7) and (III) communicate with LAMMPS to obtain interface displacements and to update the positions of the pad atoms using the continuum solution. Distribution of the mesh nodes and element quantities among processors is accomplished as follows. The values of nodal positions, velocities, accelerations, forces and nodal lumped masses are stored in *global vectors* for the entire mesh and duplicated on *every* processor. The computations involving each node or element are distributed to different processors only according to the respective node or element number, regardless of spatial position. The local computed and stored results on each processor are then shared globally using standard MPI commands [16] in order to update the global vectors associated with the mesh (see figure 3). This procedure is used because the spatial density of nodes is not uniform. The mesh (see below) is progressively coarsened moving away from the pad region toward the external surface of the continuum region to reduce the total number of degrees of freedom with no loss in quality of solution.

The parallel scheme to implement the algebraic operations necessary for equations (10)–(11) is shown in detail in figure 3(b). The diamond symbol denotes an element-wise operation between two global vectors, $\mathbf{U}$ and $\mathbf{W}$, defined for the entire mesh and duplicated on all the processors. $\diamondsuit$ is realized locally on different portions of the vectors ($\mathbf{U_1}$ and $\mathbf{W_1}$ on CPU_1, $\mathbf{U_2}$ and $\mathbf{W_2}$ on CPU_2). The results local to each processor are then combined with an *MPI_allgather* command. The scheme of figure 3(b) can be immediately extended to more

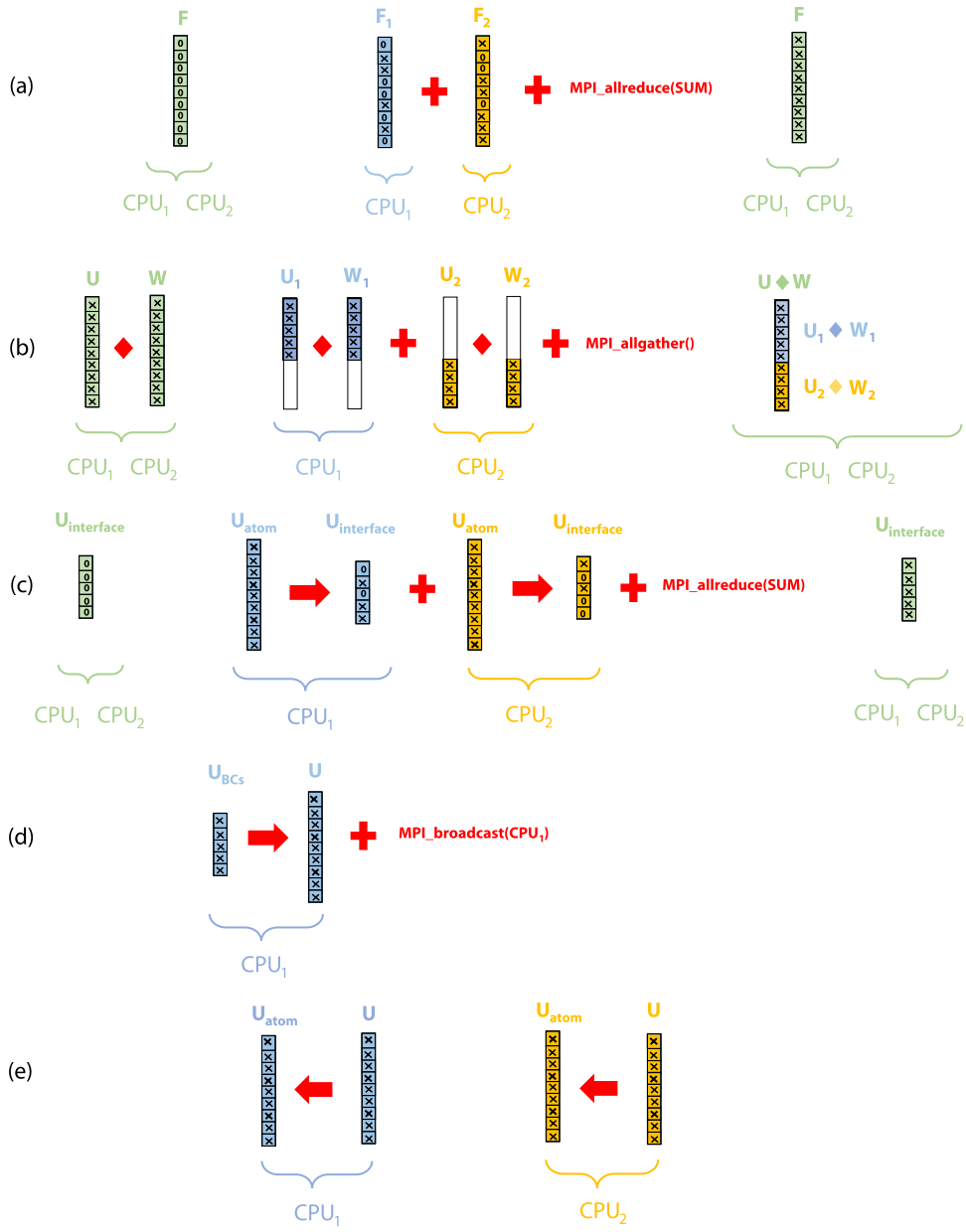

Figure 3. Parallelization scheme adopted in this work and shown for a two processors (CPU_1 and CPU_2) case: (a) Computation of nodal forces; (b) Element-wise operation between two vectors; (c) Communication of interface positions from atomistic to continuum domain; (d) Application of displacement boundary conditions to the continuum region; (e) Pad update at the end of each simulation time step.

than two vectors or to operations between a vector and a scalar. A similar approach is used in figure 3(a) to compute the vector $\mathbf{F}$ storing nodal forces due to the deformation present in the continuum region: different groups of mesh elements are assigned to each processor and the local contributions on each processor obtained using equation (7), $\mathbf{F_1}$ and $\mathbf{F_2}$, are

then combined with an *MPI_allreduce* command. Continuum and atomistic domains share information on the displacement of atoms/nodes at the interface and in the pad, as shown in figures 3(c) and (e). The values of displacement relative to the reference undeformed configuration are computed by LAMMPS for all the atoms owned locally by each processor, $\mathbf{U}_{atom}$. Thus, the displacement values of all the atoms at the interface can be directly grouped and stored in a global list owned by all the processors using an *MPI_allreduce* command, **U_I** in figure 3(c) and added to the additional displacement boundary conditions which must be satisfied by the continuum region, $\mathbf{U}_{BCs}$. Boundary conditions for the computed displacement field, **U** in figure 3(d), are imposed on the root processor and transmitted to the remaining processors through an *MPI_broadcast* command before calculation of nodal forces. Lastly, since the nodal displacements **U** are directly available on all the processors used for the LAMMPS computations, these can be directly used to update the positions of the corresponding pad atoms at the end of each simulation timestep, figure 3(e).

Although our implementation is not memory efficient due to the duplication of information allocated for each continuum degrees of freedom, it enables us (i) to balance the computational load on all the processors and, moreover, (ii) to avoid a complex mesh-nodes distribution/communication scheme requiring a non-uniform grid of processors with a mesh-dependent subdivision and the need for node redistribution during the simulation.

4. Model generation

One of the difficulties in developing FE models is the generation of an appropriate mesh for the geometry of interest. In highly accurate coupled methods, this problem is compounded by the need to have the mesh consistent with the atomistic crystal structure in the pad region adjacent to the atomistic region. When planar surfaces are constructed in atomistic systems, the under-coordinated surface atoms often do not lie on the same plane and this presents problems for many standard meshing techniques. Here we describe how to create suitable meshes for the present CADD-LAMMPS implementation described above.

CADD-LAMMPS is intended for crystalline solids. Crystals have a structure characterized by a periodic arrangement of lattice of points, with a single lattice constant a_0 for the case of a Bravais cubic lattice. The lattice constant and the elastic moduli C_{ijkl} of the crystal are dependent on the material and temperature of interest; they can be computed for a particular atomic potential directly using the standard LAMMPS code as discussed in the next section. In the present models, we start by generating a 3D cuboid atomistic cell with atoms at the positions of perfect lattice points (black in figure 4), with the cuboid axes along the desired orientations. This can be achieved by various means, including using LAMMPS itself as a pre-processor to generate a crystal structure. In general, the atomistic region may have some periodic faces, not coupled to the continuum region and other faces coupled to the continuum, as in figure 4. The lattice is extended in the directions coupled to the FE continuum to create the additional pad atoms (green in figure 4(a)). The thickness of the pad should be equal or larger than the range of the interatomic potential cutoff used in the simulation. The atoms in this cuboid are the entire domain Ω^{A+P} for the atomistic simulation. After the mesh is generated as discussed later in this section, elements having nodes superposed to lattice points in both regions Ω^A and Ω^P are used to identify atoms lying on the interface $\delta\,\Omega^I$ (red in figures 4(e) and (f)). All the atoms are input into LAMMPS and an atom-type label is used to distinguish the atoms by domain, with atom-type 1 denoting atoms inside Ω^A, atom-type 2 denoting atoms on the interface $\delta\,\Omega^I$ and atom-type 3 denoting atoms in the pad Ω^P. Usually, the atom-type is meant to distinguish different material atoms using different interatomic potentials; here the interatomic potential is the same for all atoms and the atom-type is simply a label for use in achieving the coupling.

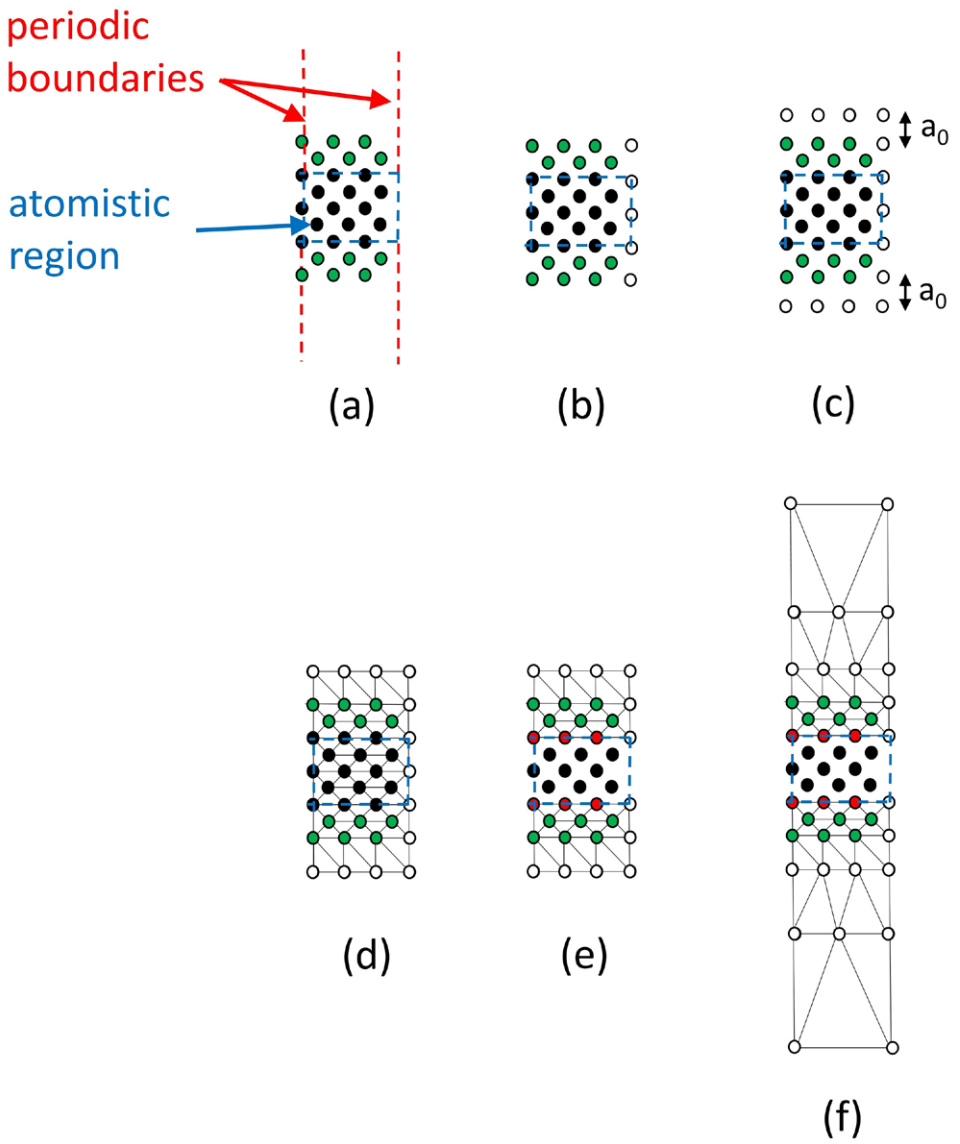

Figure 4. 2D schematics of the procedure used to generate the mesh for the CADD-LAMMPS model starting from a regular lattice of points, as presented in the text. For atoms and nodes, we use the same color scheme of figure 1. Dashed red lines identify periodic faces; blue dashed lines surround the atomistic region.

A mesh starting from the above cuboid atomistic cell is generated as follows. In the list of atoms given to LAMMPS, duplicate lattice points on the periodic faces were not included to properly describe atomic interactions across periodic boundaries and to prevent double-counting of nearest neighbors. However, these lattice points are now added to the list of points being triangulated, since they are needed to generate a mesh connecting both periodic faces, (figure 4(b)).

Table 1. Lattice constant and elastic properties in Voigt notation of an fcc aluminum cell oriented with axes in the [1 0 0], [0 1 0] and [0 0 1] lattice directions and measured according to molecular statics simulations at $T = 0$ K, with corresponding values at $T = 100$ K from [22 and 23] shown in parentheses.

	a_0 (Å)	C_{11} (GPa)	C_{12} (GPa)	C_{44} (GPa)
Ercolessi-Adams [19]	4.032 (4.039)	118.2 (109.6)	62.2 (51.6)	36.7 (29.0)
Mishin [20]	4.050 (4.050)	113.8 (111.2)	61.6 (60.3)	31.6 (32.5)

Flat rectangular surfaces are then defined at a distance a_0 from the atomic cuboid and parallel to the cuboid faces connected to the continuum. Nodes on these surfaces are then introduced as a grid of equally spaced points of spacing a_0 (figure 4(c)). These points are added to the list of atomistic/pad points and the interior and surface of this extended cuboid are then triangulated. The CGAL library [17] is used to triangulate all the points of the extended cuboid (figure 4(d)). In the extended cuboid, elements connecting only atoms in region Ω^A (type 1 atoms) can be eliminated, figure 4(e). Atoms at the interface with the continuum pad region are found from the remaining atoms of region Ω^A in the connectivity list of the remaining elements (red in the figure). The atoms, used by LAMMPS and the nodes, used by the FE, are then compared to find the pairs of atoms/nodes at the interface and in the pad that are used for communication between atomistic and continuum domains of figure 3. On the external faces of the extended cuboid there is also now a mesh of simple triangular elements on flat faces and this meshed cuboidal surface is the basis for building a mesh and finite element discretization for the rest of the continuum region of the model. Generation of the rest of the mesh in the continuum domain (with the same mesh pattern on the faces of the model in periodic directions and with progressive coarsening of the element size away from the outer regular grid of points on the boundary of the extended cuboid), figure 4(f), is achieved using any convenient mesh generator. We use the ANSYS preprocessor [18] here.

5. Validation and application

5.1. Test material and model

We exercise the code using pure aluminum as described by the embedded-atom method (EAM) interatomic potentials of Ercolessi and Adams [19] and Mishin [20], which both provide good descriptions of Al and its dislocations. The fcc lattice constant a_0 and elastic constants C_{ijkl} are computed by deforming an atomistic cell and then by computing the resulting pressure field: we use standard energy minimizations at $T = 0$ K [21] and molecular dynamics simulations in an NPT ensemble at finite temperature [22, 23]. Results are shown in table 1. Representation of the stiffness tensor in the orientation of the cuboidal simulation cell for a given simulation is achieved through standard tensor rotations [24].

We use here a thin square plate geometry for all the tests, with thickness $Z = 52$ nm, lateral dimensions $X = 4000$ nm and $Y = 4000$ nm and with periodicity assumed in the thickness direction. As shown in figure 5, the atomistic region is a cuboid embedded at the center of the plate and it has a thickness of 52 nm and lateral dimensions of respectively 18 nm and 10 nm. The remainder of the plate is treated within the continuum approximation employing 4-noded tetrahedral elements that share 4 interfaces boundaries with the atomistic domain in the X and Y directions. Different fcc lattice orientations are used for studies involving edge or screw dislocations, but always maintaining the dislocation line along the periodic Z direction. For all cases, $Y = [1\,1\,1]$ (normal to any dislocation glide plane) while the X, Z (glide and line)

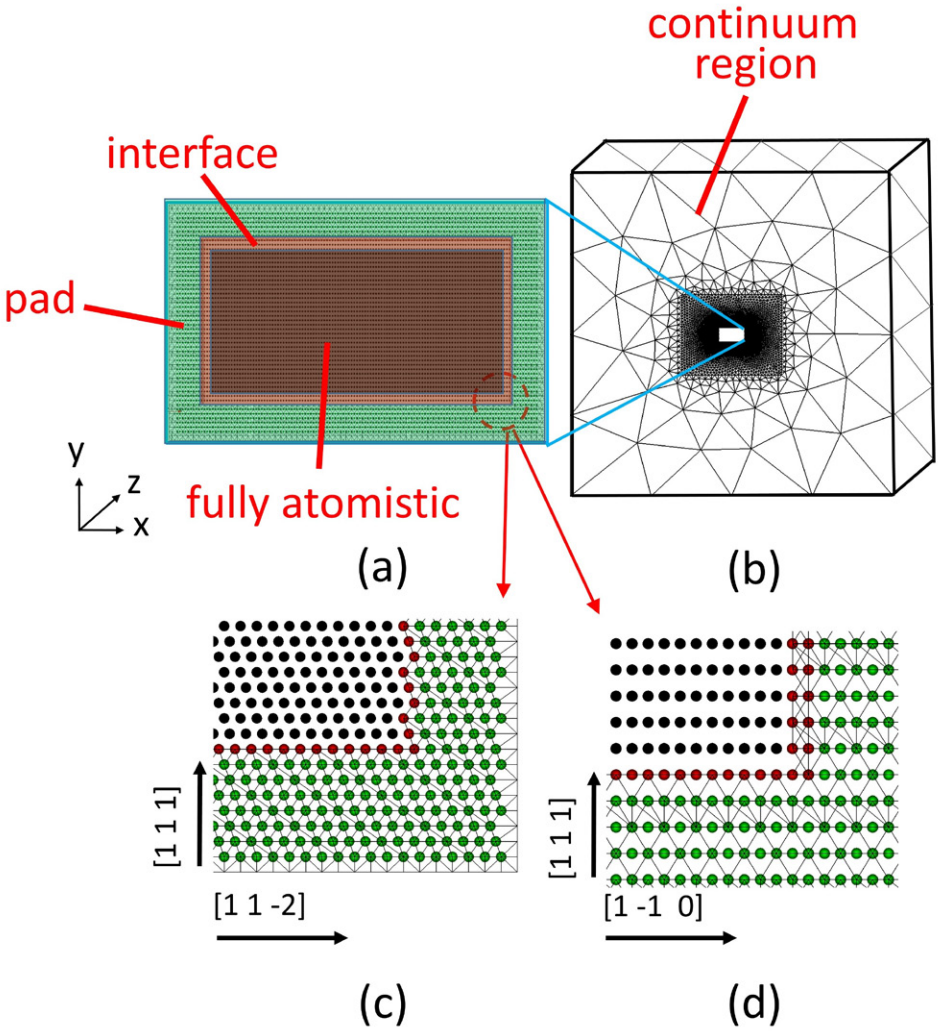

Figure 5. Model plate geometry used for validation and application, consisting of (a) an 18 nm × 10 nm atomistic region and (b) surrounding continuum region of size 4000 nm × 4000 nm discretized with tetrahedral elements. Interfaces between the two regions are present in *X* and *Y* directions and periodicity is imposed in the *Z* direction. (c) and (d) show different orientations of the fcc lattice used to study edge and screw dislocations, respectively: black atoms = bulk fcc; red atoms = atoms at the continuum/atomistic interface; green atoms = pad atoms tied to continuum nodes.

directions are [1 −1 0] [1 1 −2] and [1 1 −2] [1 −1 0] for edge and screw dislocations, respectively. The model (mesh and atomic lattice) is generated as discussed in section 4. The external faces of the continuum region have fixed displacement boundary conditions except for those faces having normal vector in the dislocation glide direction, where the model is traction-free. Since the continuum region is quite large, the differences between displacement and traction boundary conditions on the external surfaces are negligible. A fully atomistic description of the entire plate shown in figure 5 would require ∼62 billion atoms while the present model has

Table 2. Number of elements and degrees of freedom used in the models for simulations with edge and screw dislocations.

	Nodes	Elements	Pad	Atoms
Edge	2864 134	17 170 903	239 400	458 850
Screw	1288 665	7591 344	268 268	454 272

three orders of magnitude fewer atoms plus nodes, as shown in table 2. For such small sizes, computations are performed on a modest group of 128 processors.

5.2. Validation: thermodynamic stability

Explicit dynamics is essential to evolve the entire system (atomistic and continuum) at finite temperature. Explicit schemes are prone to dynamic instabilities. It has been recently shown that the CADD coupling in a fully-dynamic setting with no damping is unstable [25]. The origin of the instability is subtle and is associated solely with the mismatch in the *non-linear* behavior of the atomic and continuum domains. Here, the *non-linear* mismatch is obvious because the FE region is linear and the atoms are fully *non-linear*. However, extension of the FE region to a Cauchy–Born treatment that includes the *non-linear* response of the atoms still leads to a mismatch in the *non-linear* behavior of the two domains and thus dynamic instabilities. The instability problems can be eliminated by the introduction of damping in various ways. In CADD, we use the explicit method in the continuum primarily as a means to achieve a numerical solution to near-equilibrium or quasi-static thermomechanical problems. Therefore, damping in the continuum has no connection to the thermodynamics of the problem and can be chosen to eliminate any instabilities and also to achieve fast convergence of the overall solution. Damping in the atomistic domain must remain physical, with the Langevin dynamics tied closely to the desired thermodynamic state (temperature T) of the system. Here, we advocate the use of the 'graded stadium damping' of atoms in the atomistic domain near and at the interface, as previously proposed and validated by Qu *et al* [26] when using a quasi-static FE solution in the continuum. The 'graded stadium damping' uses Langevin terms in the equation of motion, equation (9), only for atoms in a narrow 'stadium' region of width w near the interface and with a damping coefficient that decreases linearly with increasing distance from the interface to zero just outside w. The remaining atoms inside the fully atomistic region follow Newton's law with no damping or thermostatting. The method is implemented using a Langevin damping γ function of position given by

$$\gamma(x,y) = \gamma_0\left[1 - \frac{d(x,y)}{w}\right] \qquad \text{for } (x,y) \in \Omega^A \tag{14}$$

where $d(x, y) = \max(\min(x - x_{\min}, x_{\max} - x, y - y_{\min}, y_{\max} - y, w), 0)$ is the minimum distance from the atomistic/continuum interface for an atom of the lattice at position (x, y) (here x and y are directions as in figure 5 and $x_{\min}$, $x_{\max}$, $y_{\min}$ and $y_{\max}$ define the position of the interface), γ_0 is the maximum damping in the atomistic region and is set at 20 ps^{-1},~1/2 the Debye frequency for aluminum and $w = 20$ Å is the width of the damped stadium. In Ω^A, outside the damping stadium, $d(x, y) = w$ so that $\gamma(x, y) = 0$. This 'graded stadium damping' method serves simultaneously (i) as a thermal reservoir that maintains the desired temperature and temperature fluctuations in the undamped atomistic region and (ii) as an absorbing 'low-pass filter' layer that absorbs energy emanating out toward the continuum and thus prevents wave reflection and unphysical overheating of the atomistic system.

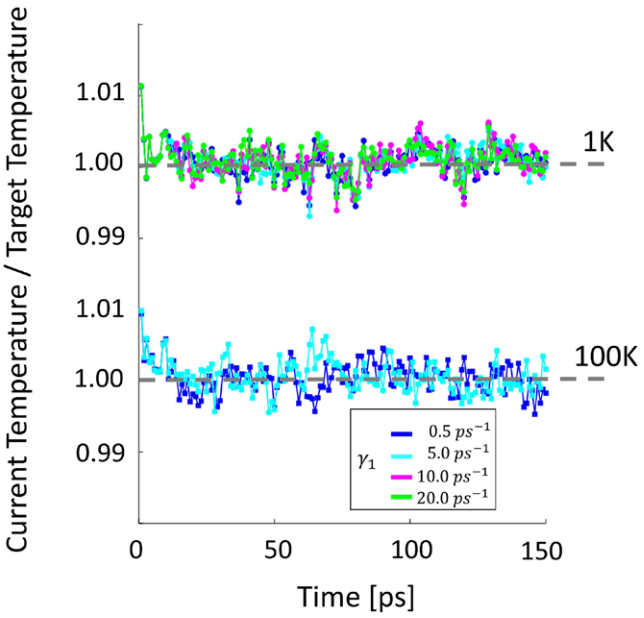

Figure 6. Normalized temperature in the undamped atomistic region versus time at $T = 1$ K and $T = 100$ K, with $\gamma_0 = 20$ ps^{-1} and for various values of damping applied in the continuum region and using the Mishin potential. Grey dashed lines indicate the desired temperature.

Figure 6 shows the normalized temperature in the atomistic region as a function of time during a simulation of an unloaded plate of Al atoms, for target temperatures $T = 1$ K and $T = 100$ K. Results are shown for different values of damping γ_1 in the continuum region to demonstrate that the treatment of the continuum has no effect whatsoever on the behavior in the atomistic regime. In all cases, the temperature in the undamped atomistic region stabilizes quickly to a steady value corresponding to the desired temperature, within the natural expected fluctuations of the finite-size atomistic domain.

The choice of damping parameter for the continuum region is important for numerical reasons because it controls the total relaxation time needed for convergence of the simulations in presence of an applied load. A good value for γ_1 is near the critical value for damping of the atomistic frequency for degrees of freedom in and around the pad region, which corresponds to a fraction of the Debye frequency. We thus generally recommend $\gamma_1 \approx \gamma_0$, here $\sim$20 ps^{-1} for Al.

The stadium damping also serves as a filter for eliminating outward-travelling waves and for preventing artificial wave reflection back into the atomistic region during dynamic simulations or dynamic events. To demonstrate the efficiency of the stadium damping method for these processes, we follow Qu *et al* [26] by investigating the time history of the atomistic domain when subjected to an initial radially-varying Gaussian displacement δr of the atoms, where the initial displacement as a function of the distance from the center of a simulation cell r is given by

$$\delta r = \frac{A}{A - u_c}(A e^{-(r/\sigma)^2} - u_c) \qquad r < r_c, \tag{15}$$

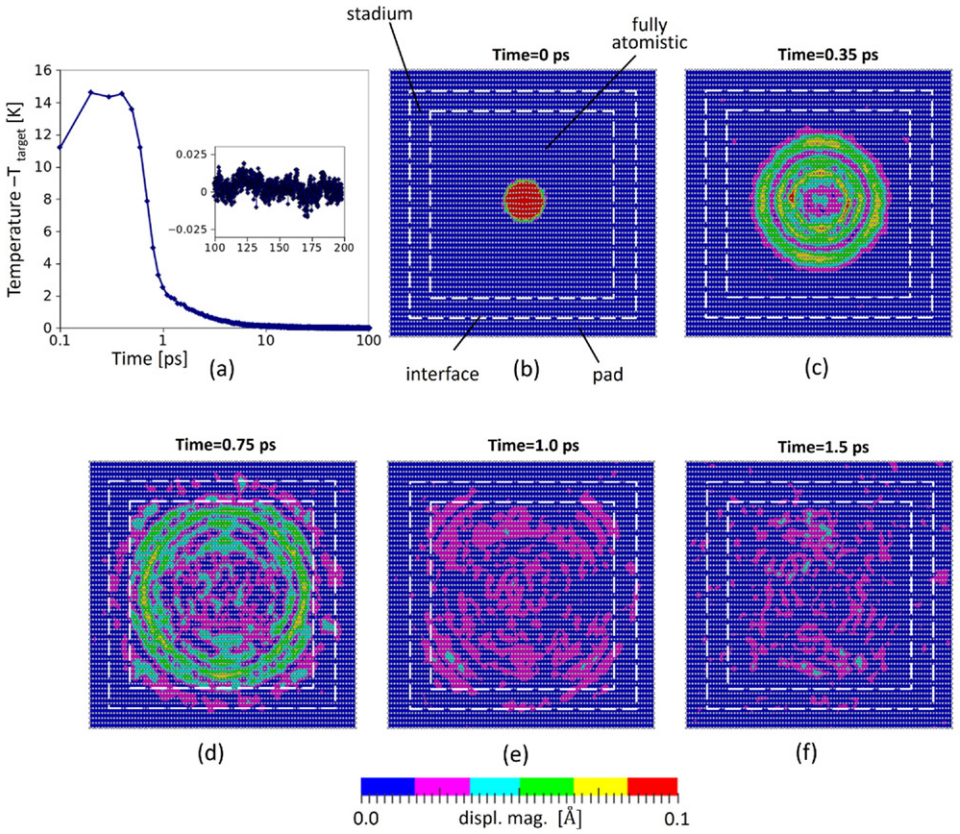

Figure 7. (a) Temperature evolution of the non-damped fully atomistic region after application of the pulse at time = 0. ((b)–(f)).Time evolution of the magnitude of displacement after application of a radial displacement pulse at the center of the atomistic region.

where $A = 0.5$ Å is the amplitude of the pulse, $\sigma = 20$ Å is the pulse width, $r_c = 10$ Å is a cut-off parameter and $u_c = Ae^{-(r/\sigma)^2}$ ensures a smooth a transition in the displacement at the cutoff value specified by r_c. We use the same outer continuum boundaries, pad width and stadium parameters specified earlier, but here we test a fully atomistic region of 60 Å × 60 Å with a distance of 100 Å between the periodic faces. Before application of the pulse, the atomistic region is fully equilibrated at $T = 1$ K. Figure 7 shows the evolution through time, with the displacement applied at $t = 0$, of the magnitude of displacement relative to the reference perfect lattice. The contour plots are drawn on a plane slicing the atomistic region at its center and normal to the periodic direction and the spheres represent the atoms of the atomistic region projected on this plane. The dynamic waves propagate outward and are damped as they enter the stadium region, with no visual evidence of wave reflections. Residual energy, created well before the first waves reach the stadium region and due to the complexity and non-linearity of the deformation, remains in the atomistic region well after the outgoing waves have been absorbed/damped by the stadium. Figure 7 shows the time evolution of the excess temperature due to the pulse and the temperature decays steadily back to the equilibrium value over time.

5.3. Validation: accuracy of interface coupling

To assess the accuracy of the interface coupling under quasi-static conditions, we evaluate the spurious forces acting on a dislocation as it approaches the atom/continuum interface. The long-range elastic field of the dislocation extends across the atom/continuum boundary and thus any errors in representation of the dislocation field generate artificial 'image' stresses. Such errors can be generated by (i) poor coupling methodology, (ii) non-linear response that is not captured by the linear FE approximation, or (iii) rapid field gradients that are not accurately captured by the FE mesh and FE displacement shape functions. As a dislocation approaches the atom/continuum interface, each of these artificial forces is expected to increase since the dislocation core itself is a region of intrinsic non-linear materials response with high stresses and high stress gradients.

We analyze the quality of the method by inserting a dislocation into the center of the atomistic domain using the displacement field of the isotropic Volterra field as initial guess, relaxing the system to achieve the correct atomistic core and then loading the plate in shear to drive the dislocation toward the atom/continuum interface. When the applied shear stress exceeds the Peierls stress, the dislocation begins to glide. In an infinite system, the glide should continue forever, since there are no other forces on the dislocation. In the coupled system, any artificial or spurious repulsive forces caused by the coupling can act on the dislocation and cause it to stop when the net driving force (applied force plus spurious forces) falls below the Peierls stress. Measurement of the position of the dislocation as a function of the applied stress then allows for a precise determination of the magnitude of the spurious forces, in terms of a stress, at the position of the halted dislocation. Figure 9 shows an edge dislocation using the Mishin EAM potential that has been halted very near the interface by spurious forces; the applied stress must be increased further to continue the glide toward the interface. Our goal here is to measure the magnitude of these spurious forces as a function of distance from the interface. The present work does not address the seamless passing of dislocations from atomistic to continuum domain as realized in the original 2D CADD implementation; here we provide only the accurate displacement-coupling methodology, working in 3D and fully integrated with LAMMPS.

Details of the simulation are as follows. For the single dislocation in the atomistic domain, we use the superposed analytic and finite element solutions discussed in section 2 and figure 2 to find the positions of the mesh nodes, explicit dynamics at $T = 1$ K (equations (10) and (11)) and an integration time-step $\Delta t = 1$ fs. To avoid any artificial pinning of the dislocation by the graded stadium damping, we instead use a constant damping parameter of 1.0 ps^{-1} throughout the entire atomistic domain to control the temperature and a damping parameter of 16.0 ps^{-1} in the continuum region. The system is first relaxed for 500 ps without additional loads applied to the outer boundary of the continuum region to allow the elastic waves to transport the deformation information imposed at the external boundaries into the atomistic region. Then, small uniform shear strain increments are used to generate an effective shear stress by displacing atoms and nodes with respect to the dislocation glide plane. The system is fully relaxed after each load increment and, for all practical considerations, the loading method corresponds to a quasi-static test. After relaxation at zero stress, the dislocations dissociate into two partials separated by a stacking fault. As is well-known, the dissociation distance is larger for the Ercolessi–Adams potential as compared to the Mishin potential due to the higher stable stacking fault energy for the Mishin potential. The Peierls stress at $T = 0$ K for an edge dislocation is 2–3 MPa for both EAM potentials used here. At $T = 1$ K, thermal energy is sufficient to reduce the Peierls stress to nearly zero. The Peierls stress at $T = 0$ K for a screw dislocation is 16–18 MPa and 33–35 MPa for the Ercolessi–Adams and Mishin EAM potentials, respectively. At $T = 1$ K, these are reduced to 9 and 30 MPa respectively.

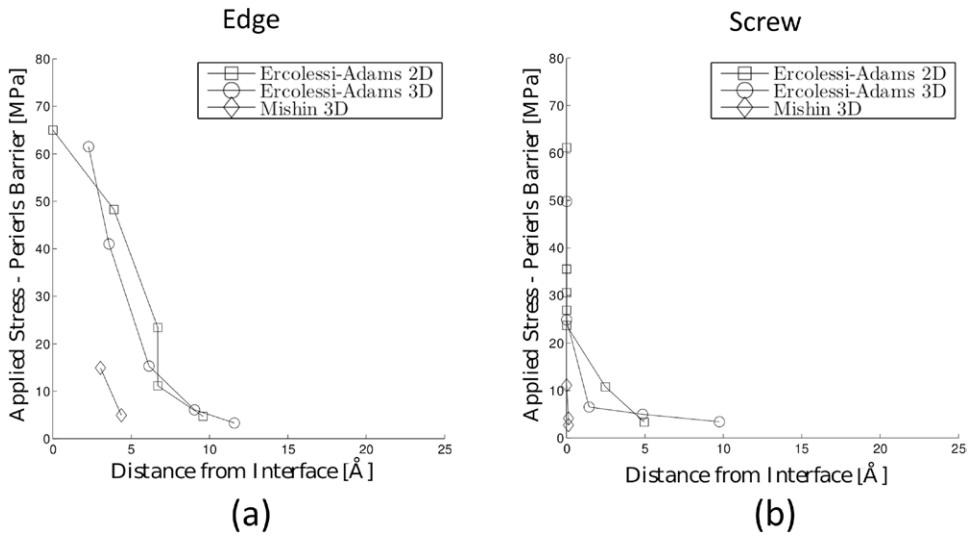

Figure 8. Close-up of an edge dislocation in the atomistic region at a distance X from interface for some value of effective applied shear stress above the Peierls barrier. The atoms of the dislocation are highlighted using Common Neighbor Analysis (stacking fault in blue and partials in purple). The same color coding of figure 1 is used for atoms in the fully atomistic region (black), at the interface (red) and in the pad (green).

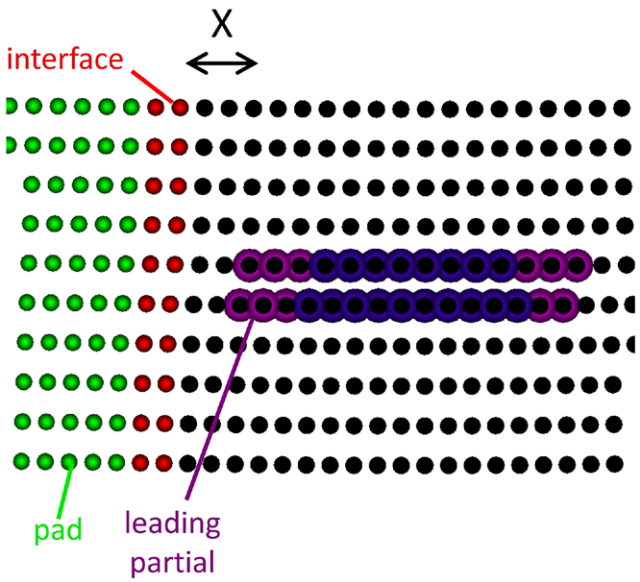

Figure 9. Spurious force versus dislocation distance (measured from the leading partial) from the atom/continuum interface. Results for the 3D model are compared to the values measured by Dewald *et al* in 2D [27]. Spurious forces on atomistic dislocations peak at the interface and become important only for distances smaller than 10 Å from the continuum region.

At stresses above the Peierls stress, the dislocations move and then halt due to the spurious forces, as discussed above. Figure 8 shows the halting position of the leading partial of

edge and screw dislocations as a function of the applied stress minus the Peierls stress, which is equal to the spurious stress. For edge dislocations, spurious repulsive forces are below a few MPa for dislocations beyond 10 Å for the Ercolessi–Adams potential with a edge dissociation width of ∼15 Å and beyond 5 Å for the Mishin potential with a edge dissociation width of ∼13 Å. For screw dislocations, spurious forces are below a few MPa at distances between 5–10 Å for the Ercolessi–Adams potential (dissociation width ∼10 Å) and at distances beyond ∼1 Å for the Mishin potential (screw dissociation width ∼9 Å). Also shown are previous results obtained for the Ercolessi–Adams potential using the 2D plane-strain implementation of CADD [27], which is expected and found to be nearly identical to the 3D implementation here. We conclude that the multiscale coupling generates non-physical forces exceeding a few MPa on dislocations only at distances less than ∼10 Å from the interface for all the cases studied. In applications of the CADD-LAMMPS method, we therefore recommend that studies be designed so that dislocations remain further than 15 Å from the interface. This also enables the implementation of the 'graded stadium damping' method with $w = 15$ Å in the glide directions without any undue influence on dislocation motion. The 'passing' of dislocations from atomistic to continuum, a key and unique feature of the original CADD model, is not addressed here although we are developing algorithms to enable full 3D coupling of atomistic and discrete dislocation methods.

5.4. Application: dislocation bow-out

Here we apply the code to study one non-trivial problem, the quasi-static bowing out of a dislocation pinned by obstacles [28–32] and compare our multiscale results (effectively infinite crystals) to standard finite-size atomistic simulations with roughly comparable numbers of degrees of freedom. As in the previous section the dislocation is fully confined in the atomistic region during all the bowout process, thus there is no need to address the 3D passing of the dislocation from atomistic to continuum domain. The interaction of dislocations with obstacles is one important source of strengthening in a metal. When the obstacles are precipitates intentionally designed by alloying, such strengthening is desirable and the object of alloy design. When the obstacles are defects formed by damage processes, for example during irradiation, such strengthening is undesirable because it is associated with reduced ductility of the material. Thus, there are many atomistic studies in the literature that aim to quantify the role of different types of obstacles on the inhibition of dislocation glide and the consequent strengthening. As computational metallurgy seeks to be increasingly quantitative, it is important that simulations be accurate and reliable and thus eliminate unphysical effects due to simulation size and image forces. In addition, the validation of theoretical models for dislocation/obstacle interactions as a function, for instance, of obstacle size and spacing, requires that the atomistic simulations provide accurate results. In fact, unphysical effects can cause atomistic simulations to deviate from anticipated scaling behavior and this can be incorrectly interpreted as failure of the theory. Here, we only analyze bow-out configurations under increasing applied stress with idealized pinning obstacles. We do not consider the breaking away of the dislocation from the obstacles because the purpose here is only a demonstration and not a metallurgical quantification. A forthcoming analysis of results obtained here will be used to determine the appropriate 'line tension' and/or 'core energy' for curved dislocations represented by various interatomic potentials [34].

For the multiscale simulations, we use the atomistic cell described in the previous section and insert an initial dislocation in the same manner. Immobile rigid obstacles are inserted after the initial relaxation of the system by simply fixing the atomic positions of a set of atoms corresponding to a small prismatic shape of dimensions 2.5 nm along X (to fix all atoms along

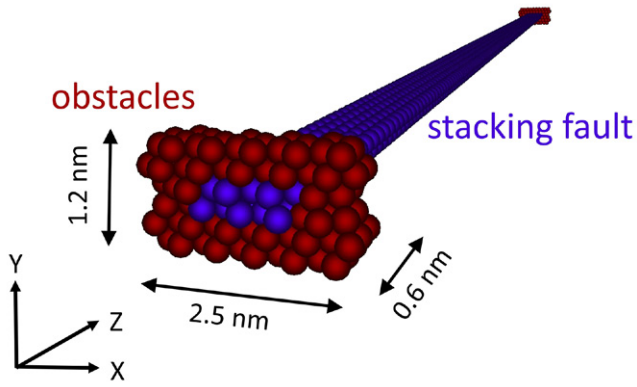

Figure 10. Obstacles, in brown, pinning the dislocation stacking fault, in blue. Periodic boundaries are used in the *Z* direction.

the dissociated core), 1.2 nm along *Z* and 1.2 nm along *Y*, as indicated by the brown-colored atoms in figure 10. Fixing the atom positions corresponds to setting the forces and velocities to zero at each time step during the simulation. Loading is achieved by applying increments of shear displacement to the outer surface of the plate model, as described earlier. For the finite-size standard atomistic simulations, we use the 'Periodic Array of Dislocations' (PAD) approach. The atomistic simulation cell has free surfaces in direction *Y* normal to the glide plane and periodicity in both the dislocation glide (*X*) and line (*Z*) directions, following the procedure developed by Osetsky *et al* [29] and by Rodney [32] for edge and screw dislocations. We use dimensions of 20 nm in *Y*, 20 nm in *X* and 52 nm in *Z*. The obstacles are inserted in the same manner. Explicit dynamics at $T = 1$ K is used for both simulations.

Multiscale and finite-size simulation results for the bowout shape of edge and screw dislocation pinned segments of 52 nm are shown in figure 11, where the dislocation visualization is achieved by showing only a line representing the averaging positions of the atoms in the stacking fault. As expected, pinned dislocations bow-out under load into elliptic (almost circular) arcs but with occasional kinks oriented at 60 degrees with respect to the original dislocation line. The kinks are more evident at small values of shear stress where the discreteness of the lattice prevents the bow-out from following a smooth continuous curve that would be expected in a continuum model. Results are comparable for both EAM potentials, although this is difficult to assess because the results shown were obtained at different applied stresses. In general, edge dislocations bow out approximately twice as much as screw dislocations at similar applied loads, consistent with the expected lower line tension of edge dislocations relative to screw dislocations. However, continuum models that include only elasticity suggest that the line tension of an edge dislocation should be approximately 1/4 that of the screw and the corresponding bow-out should thus be 4 times larger. Our results here suggest that the actual ratio of edge to screw line tension is $\sim$1/2. More detailed interpretation of the bow-out, line tensions, core energies and the role of kinks and Peierls stresses, will be addressed in a future publication [34]. Of interest here is the difference between the multiscale result, which is completely free of any boundary-induced image forces on the dislocation and the finite-size atomistic simulation. The presence of free surfaces and periodic images in the glide direction generally reduces the bow-out in the atomistic PAD model for the *edge* dislocation, relative to the (true) multiscale result. The image forces act against bow-out, thus requiring larger applied stresses to achieve the same level of bow-out as obtained in the multiscale simulation.

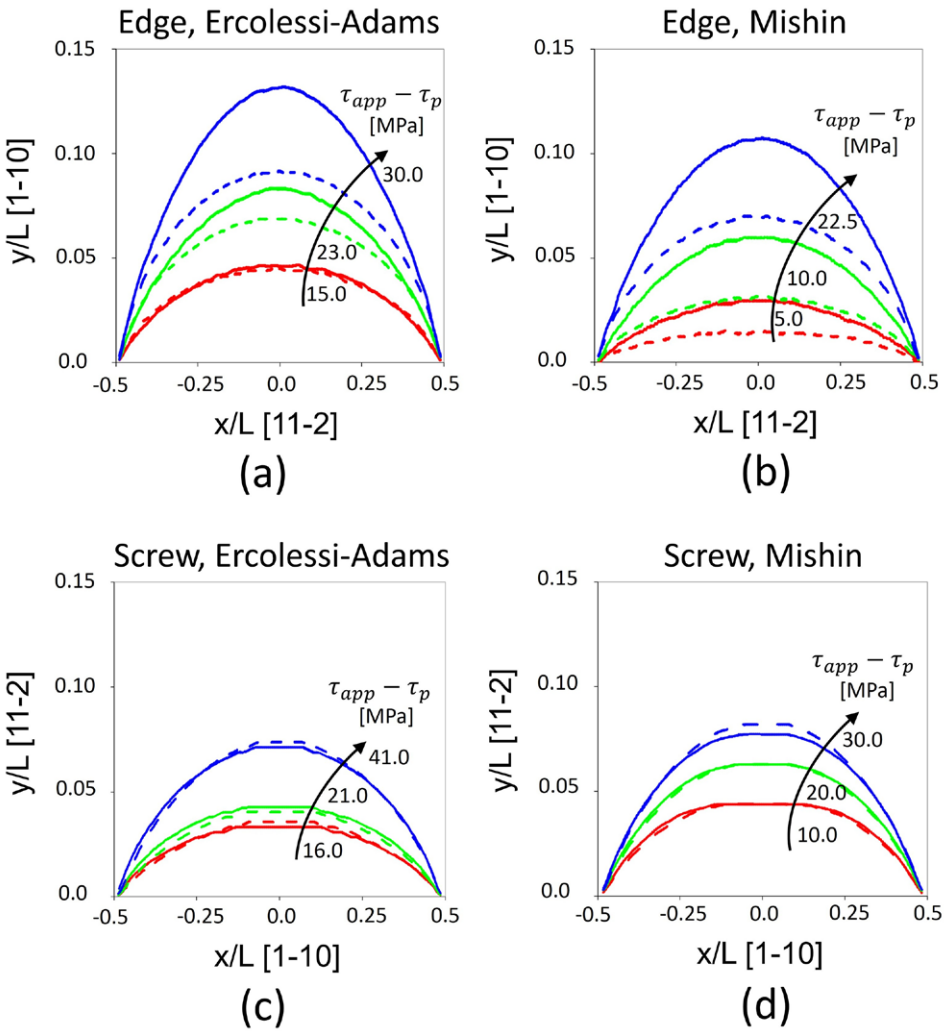

Figure 11. Bowout shape for multiscale (continuous line) and finite size (dashed lines) simulations for Ercolessi–Adams edge (a) and screw (c) dislocation and Mishin edge (b) and screw (d) dislocations.

Somewhat surprisingly, the atomistic and multiscale results for the *screw* dislocation are quite comparable, suggesting minimal image forces for this particular atomistic PAD simulation size. We have recently presented an analysis of the image stresses due to finite size atomistic cells and have shown that the image forces for the screw are quite reduced relative to those for the edge and that the aspect volume used here for the atomistic PAD simulations is in the range that generates the smallest image forces for both edge and screw dislocations [33]. Thus, for this problem, the multiscale approach is necessary to capture correct behavior for both edge and screw at the same time and to achieve quantitative accuracy for the edge dislocation. Larger atomistic cells can always be used and analysis shows that the image forces scale inversely with the volume, but larger sizes are more costly, particularly for parametric studies. Finally, in more complex problems, for instance involving multiple dislocations, dislocations with non-ideal orientations relative to the simulation cell and/or cracks, the role of

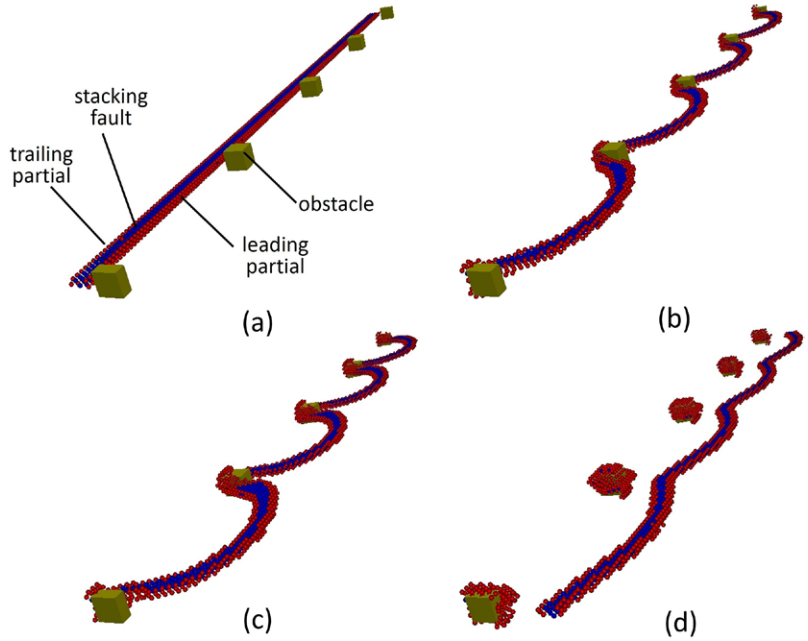

Figure 12. Dislocation gliding past an array of rigid obstacles.

the simulation cell size would be far more difficult to assess while application of the multi-scale model eliminates any and all unphysical effects from the simulation.

Finally, to demonstrate another fully dynamic (transient) situation, we present results for a dislocation moving past the set of obstacles and leaving behind Orowan loops. The obstacles exist as before and we use the Mishin potential. An initial screw dislocation is introduced on the central glide plane but now a short distance behind the obstacles. A shear displacement corresponding to a resolved shear stress of 240 MPa is applied to initiate dislocation gliding. At this load, the dislocation first glides while remaining straight, figure 12(a), becomes pinned by the obstacles and starts to bowout, figure 12(b) and then the screw dislocation starts to overcomes the rigid obstacles by initiating a cross-slip mechanism, figure 12(c). The dislocation then depins from the obstacles and continues to move forward along the glide plane. The final depinning appears to be controlled by the interaction between different portions of the bowed out leading partial and leaves a residual stacking fault around the obstacles, corresponding to an Orowan looping mechanism, figure 12(d). This example simply demonstrates the fully dynamic operation of the code within a standard materials science problem, but with artificial obstacles that make detailed analysis unproductive. Future users of the code can execute similar computations using realistic obstacles of various types, with full confidence in the quality of the simulation results, whether quasi-static or dynamic.

6. Summary

We have presented an extension of the multiscale coupling scheme used in the 2D Coupled Atomistic/Discrete-Dislocation method to 3D simulation cells and implemented within the large-scale parallel molecular dynamics code LAMMPS to take advantage of the many tools and atomic potentials in this popular open-source code. In particular, we have described the

algorithm for parallel computing and mesh development for the execution of the continuum finite element method in a very large region surrounding a central atomistic domain using an explicit method. We have verified dynamic stability of suitably-thermostatted finite-temperature systems and demonstrated the high fidelity of the coupling through analysis of the forces on gliding dislocations. As a first example application, we have examined quasi-static dislocation bowing around obstacles and shown differences with standard finite-size atomistic simulations. As means to fully test the dynamic capabilities of our code we have additionally demonstrated that the stadium-damping thermostat can absorb outgoing dynamic waves with no detectable artificial reflection of energy back into the atomistic domain. We have also examined the dynamic glide and depinning of a dislocation encountering an array of obstacles. Our implementation allows for the simulation of extremely large models with atomic precision in the central atomistic domain at a fraction of the cost of comparably-sized fully atomistic models, as typical of multiscale models, thus allowing us to obtain results for effectively infinite atomic lattices.

Future work could improve on the scalability of the code and the efficiency of the parallel schemes shown here to further diminish the computational costs of large multiscale simulations. The development of a library of meshes for different problems is also a valuable future undertaking. The method operates using a fixed domain and is thus not automatically adaptive. However, adaptivity is easily achieved by creating a library of systems having successively-larger atomistic domains and then simply transferring all information (atom and node displacements and velocities, with appropriate interpolation) from one size to the next larger size. A simple detection algorithm can be developed, analogous to the previous CADD method, to determine when deformations near the atom/continuum interface have reached a value at which the larger size atomistic domain is necessary. While not as elegant as on-the-fly adaptive methods, such as the Quasicontinuum Method, the present approach has the benefit of highly accurate coupling, parallel operation within LAMMPS and general ease of use. While there are competing methods and codes, these mainly exist as research-level codes within individual research teams. We hope our development here will permit a wide array of researchers to use the CADD-LAMMPS code because of its implementation in LAMMPS. To this end, our documented *fix* for LAMMPS will be provided to the LAMMPS developers for inclusion within the open-source LAMMPS environment.

Acknowledgments

The authors gratefully acknowledge support of this work by the Swiss National Foundation through the grant 513247 entitled ‘Coupled Atomistic/Discrete-Dislocations in 3d’. The authors also acknowledge R Miller, D Warner and J F Molinari for insightful discussions during the realization of this work. The authors also thank B Szajewski (Brown/EPFL) for interactions associated with application of the method and T Junge, N Richart, J Cho, G Anciaux in the LSMS Lab of J F Molinari at EPFL for suggestions during implementation of the code.

References

[1] Miller R E and Tadmor E B 2007 Hybrid continuum mechanics and atomistic methods for simulating materials deformation and failure *MRS Bull.* **32** 920–6
[2] Miller R E and Tadmor E B 2009 A unified framework and performance benchmark of fourteen multiscale atomistic/continuum coupling methods *Modelling Simul. Mater. Sci. Eng.* **17** 053001
[3] Plimpton S 1995 Fast parallel algorithms for short-range molecular dynamics *J. Comput. Phys.* **117** 1–9

[4] Espanol M, Kochmann D M, Conti S and Ortiz M 2013 A Γ-convergence analysis of the quasicontinumm method *Mod. Simul. Mater. Sci. Eng.* **11** 766–94
[5] Kochmann D M and Venturini G N 2014 A meshless quasicontinuum method based on local maximum-entropy interpolation *Mod. Simul. Mater. Sci. Eng.* **22** 034007
[6] Shiari B, Miller R E and Curtin W A 2005 Coupled atomistic/discrete dislocation simulations of nanoindentaion at finite temperature *Trans. ASME* **127** 358–68
[7] Shilkrot L E, Miller R E and Curtin W A 2002 Coupled atomistic and discrete dislocation plasticity *Phys. Rev. Lett.* **89** 025501
[8] Shilkrot L E, Curtin W A and Miller R E 2002 A coupled atomistic/continuum model of defects in solids *J. Mech. Phys. Solids* **50** 2085–106
[9] Shilkrot L E, Miller R E and Curtin W A 2004 Multiscale plasticity modeling: coupled atomistics and discrete dislocation mechanics *J. Mech. Phys. Solids* **52** 755–87
[10] Zienkiewicz O C and Taylor R L 1967 *The Finite Element Method* **1** –2, 5th ednNew York McGraw-Hill
[11] Van der Giessen E and Needleman A 1995 Discrete dislocation plasticity: a simple planar model modelling *Modelling Simul. Mater. Sci. Eng.* **3** 689–735
[12] Kubin L and Canova G 1992 The modeling of dislocation patterns discrete dislocation plasticity: a simple planar model modelling *Scr. Metall. Mater.* **27** 957–62
[13] Zbib H M, Rhee M and Hirth J P 1998 On plastic deformation and the dynamics of 3D dislocations *Int. J. Mech. Sci.* **40** 113–27
[14] Schwarz K W 1997 Interaction of dislocations on crossed glide planes in a strained epitaxial layer *Phys. Rev. Lett.* **78** 4785–8
[15] Hirth J P and Lothe J 1982 *Theory of Dislocations* 2nd edn (New York: Wiley)
[16] Gabriel E *et al* 2004 Open MPI: goals, concept and design of a next generation MPI implementation *Proc., 11th European PVM/MPI Users' Group Meeting* (*Budapest, Hungary*) pp 97–104
[17] CGAL, Computational Geometry Algorithms Library www.cgal.org
[18] ANSYS Academic Research, Release 15.0
[19] Ercolessi F and Adams J B 1994 Interatomic potentials from first-principles calculations: the force-matching method *Europhys. Lett.* **26** 583–97
[20] Mishin Y, Farkas D, Mehl M J and Papaconstantopoulos D A 1999 Interatomic potentials for monoatomic metals from experimental data and *ab initio* calculations *Phys. Rev.* B **59** 3393
[21] Polak B and Ribiere G 1969 Note surla convergence des methodes de directions conjuguees *Rev. Fr. Imform. Rech. Oper.* **16** 35–43
[22] Yamakov V I, Warner D H, Zamora R J, Saether E, Curtin W A and Glaessgen E H 2014 Investigation of crack tip dislocation emission n aluminum using multiscale molecular dynamics and continuum modeling *J. Mech. Phys. Solids* **65** 35–53
[23] Warner D H and Curtin W A 2009 Origins and implications of temperature-dependent activation energy barriers for dislocation nucleation in face-centered cubic metals *Acta Mater.* **57** 4267–77
[24] Ting T C T 1996 *Anisotropic Elasticity: Theory and Applications* (Oxford: Oxford University Press) pp 53–6
[25] Junge T and Molinary J F 2014 Modelling plasticity in nanoscale contact EPFL *PhD Thesis*, Lausanne, Switzerland
[26] Qu S, Shastry V, Curtin W A and Miller R E 2005 A finite–temperature dynamic coupled atomistic/discrete dislocation method *Modelling Simul. Mater. Sci. Eng.* **13** 1101–18
[27] Dewald M and Curtin W A 2006 Analysis and minimization of dislocation interactions with atomistic/continuum interfaces *Modelling Simul. Mater. Sci. Eng.* **14** 497–514
[28] Bacon D J, Osetsky Y N, Rodney D 2009 Dislocation obstacle interactions at the atomic level *Dislocations in Solids* ed J P Hirth and L Kubin (Amsterdam: Elsevier) pp 1–90
[29] Osetsky Y N and Bacon D J 2003 An atomic-level model for studying the dynamics of edge dislocations in metals *Modelling Simul. Mater. Sci. Eng.* **11** 427–46
[30] Osetsky Y N and Bacon D J 2005 Comparison of void strengthening in fcc and bcc metals: large-scale atomic-level modelling *Mater. Sci. Eng.* A **400** 374–7
[31] Rodney D and Martin G 2000 Dislocation pinning by glissile interstitial loops in a nickel crystal: a molecular-dynamics study *PhyS. Rev.* B **61** 8714–25
[32] Rodney D 2004 Molecular dynamics simulation of screw dislocations interacting with interstitial frank loops in a model FCC crystal *Acta Mater.* **52** 607–14
[33] Szajewski B A and Curtin W A Analysis of spurious image forces in atomistic simulations of dislocations *Modelling Simul. Mater. Sci. Eng.* **23** 025008
[34] Szajewski B A, Pavia F Curtin W A Atomic scale calculation of dislocation line tension (in preparation)